Journal of Computational Physics 230 (2011) 5399–5416

Contents lists available at ScienceDirect

Journal of Computational Physics

journal homepage: www.elsevier.com/locate/jcp

# On the development of a high-order compact scheme for exhibiting the switching and dissipative solution natures in the Camassa–Holm equation

Tony W.H. Sheu [a,b,c,*], P.H. Chiu [d], C.H. Yu [a]

[a] Department of Engineering Science and Ocean Engineering, National Taiwan University, Taipei, Taiwan, ROC
[b] Center for Quantum Science and Engineering (CQSE), National Taiwan University, Taipei, Taiwan, ROC
[c] Taida Institute of Mathematical Sciences (TIMS), National Taiwan University, Taipei, Taiwan, ROC
[d] Nuclear Engineering Division, Institute of Nuclear Energy Research, Taoyuan County, Taiwan, ROC

ARTICLE INFO

*Article history:*
Received 23 September 2010
Received in revised form 22 March 2011
Accepted 23 March 2011
Available online 1 April 2011

*Keywords:*
Camassa–Holm equation
Fifth-order spatially accurate
Long-term accurate
Symplecticity
Conservation of Hamiltonians
Switching scenario
Peakon–peakon
Dissipative scenario
Peakon–antipeakon

ABSTRACT

In this paper a two-step iterative solution algorithm for solving the Camassa–Holm equation, which involves only the first-order derivative term, is presented. In each set of the $u-P$ and $u-m$ differential equations, one is governed by the inviscid nonlinear convection–reaction equation for the time-evolving fluid velocity component along the horizontal direction. The other equation is known as the inhomogeneous Helmholtz equation. The resulting reduction of differential order facilitates us to develop the flux discretization scheme in a stencil with comparatively fewer points. For accurately predicting the unidirectional propagation of the shallow water wave, the modified equation analysis for eliminating several leading discretization error terms and the Fourier analysis for minimizing a particular type of wave-like error are employed. In this study, the fifth-order spatially accurate combined compact upwind scheme is developed in a three-point stencil for approximating the first-order derivative term. For the purpose of retaining a long-term accurate Hamiltonian and multi-symplectic geometric structures in Camassa–Holm equation, the time integrator (or time-stepping scheme) chosen in this study should conserve symplecticity. Another main emphasis of conducting the present calculation of Camassa–Holm equation is to shed light on the conservation of Hamiltonians up to the time before wave breaking. We also intended to elucidate the switching scenario by virtue of the peakon–peakon interaction problem and the dissipative scenario after the time of head-on collision in the peakon–antipeakon interaction problem.



## 1. Introduction

The nonlinear Camassa–Holm (CH) equation, which was firstly derived by Camassa and Holm [1] for modeling the unidirectional propagation of irrotational waterwave over a planar wall, will be numerically investigated in this study. Like the Korteweg–de Vries (KdV) equation derived by performing the asymptotic expansion on the Euler shallow water equation, the CH equation given by

$$u_t + 2\kappa u_x - u_{xxt} + 3uu_x = 2u_x u_{xx} + uu_{xxx} \tag{1}$$

* Corresponding author at: Department of Engineering Science and Ocean Engineering, National Taiwan University, Taipei, Taiwan, ROC. Tel.: +886 2 33665746; fax: +886 2 23929885.
*E-mail address:* twhsheu@ntu.edu.tw (T.W.H. Sheu).

0021-9991/$ - see front matter © 2011 Elsevier Inc. All rights reserved.
doi:10.1016/j.jcp.2011.03.043

was derived by using a different shallow water approximation in the inviscid limit. Based on the shallow-water theory, the positive constant $\kappa$ was derived to be $\kappa = (gh_0)^{1/2}$, where $g$ stands for the gravity and $h_0$ is denoted as the undisturbed water depth. When $\kappa$ is equal to 0, Eq. (1) is referred to as the hyperelastic-rod wave equation [2]. As $t > 0$ and $\kappa = 0$, Eq. (1) turns out to be the special case of the $b$-family partial differential equation $u_t - u_{xxt} + (b+1)uu_x = bu_xu_{xx} + uu_{xxx}$ [3]. This equation is integrable for $b = 2$ and 3, which correspond respectively to the Camassa–Holm equation and the Degasperis–Procesi equation [4].

The Camassa–Holm equation has been the subject of intensive investigation because of the possible generation of breaking and peaked solitary waves. The initially smooth solution may be evolved to develop singularities in finite time in the form of a breaking wave [5,1] or peakons [1] due to the embedded nonlinear terms. In the presence of peakon solution, the CH solution computed at $\kappa = 0$ is no longer smooth. At the crest, the solution with a discontinuous first derivative will be exhibited. Besides the mathematical beauty in the investigated third-order dispersive partial differential equation and its practical relevance to shallow water and scattering wave problems, nonlinear CH equation catches our attention because this equation permits formation of non-smooth solitary wave solutions. In the limit of $\kappa \to 0$, breaking of the solution smoothness at the peak of each peakon can result in a sharply changed water wave profile at the cusp of peakon. At these peaks, the numerically introduced high-frequency dispersion error can considerably deteriorate the simulation quality [6].

The third-order nonlinear dispersive equation (1) has several rich geometric structures. The fact that CH equation can be completely integrated by means of its associated Lax pair is one of many intriguing properties. Since CH equation is classified to be multi-symplectic, Eq. (1) can be rewritten as a system of first-order equations given by $\underline{\underline{M}}\underline{z}_t + \underline{\underline{K}}\underline{z}_x = \nabla_z S(z)$ for a state-variable vector $\underline{z}$. Note that the scalar function $S$ is smoothly dependent on $\underline{z}$. The two square matrices $\underline{\underline{M}}$ and $\underline{\underline{K}}$, which are skew-symmetric, define the symplectic structure given by $(\bar{\omega}, \bar{\kappa})$, where $\bar{\omega} = d\underline{z} \wedge \underline{\underline{M}} d\underline{z}$ and $\bar{\kappa} = d\underline{z} \wedge \underline{\underline{K}} d\underline{z}$. According to the work of Bridges and Reich [7], the derived pair of variables $(\bar{\omega}, \bar{\kappa})$ conserves symplecticity in the sense of $\frac{\partial \bar{\omega}}{\partial t} + \frac{\partial \bar{\kappa}}{\partial x} = 0$. Thanks to this multi-symplectic conservation law, one can define, at least, four density functions. The resulting local conservation laws and the globally conserved quantities have been derived in [8]. Given an initial condition $u_0(x, t = 0) \in H^1$, where $H^1$ is the Sobolev space, the CH equation investigated at $\kappa = 0$ has been shown to possess the well-known conservation law $M = \int_{-\infty}^{+\infty} u\,dx = constant\ c_1$. The other two distinguished conservation quantities are known as $\frac{1}{2}\int_{-\infty}^{+\infty}(u^2 + u_x^2)dx = constant\ c_2$ (Hamiltonian $H_1$) [9–11] and $\frac{1}{2}\int_{-\infty}^{+\infty}(u^3 + uu_x^2 + 2\kappa u^2)dx = constant\ c_3$ (Hamiltonian $H_2$) [9,12,13]. Note that the Hamiltonian $H_1 = \frac{1}{2}\int_{-\infty}^{+\infty}(u^2 + u_x^2)dx$ has an association with the energy density $u^2 + u_x^2$. For a detailed discussion of the possible conservation laws embedded in the CH equation, we refer the reader to the paper by Lenells [14].

Prior to the breaking of wave, it is essential to numerically conserve $H_1$ since the Camassa–Holm equation satisfies the least action principle [11,15]. Because Eq. (1) allows formation of a solution that is global in time and permits wave-breaking solutions, this study will address the solution behavior at a time immediately after wave breaking. We are aiming to gain some insights into the wave breaking process to clarify if a switching or an annihilation scenario [11,16] will take place through the analysis of the peakon–antipeakon interaction problems.

At $\kappa = 0$, Eq. (1) has a bi-Hamiltonian structure [17]. The CH equation admits exact solution, which is represented by the canonical coordinates $p$ and $q$ as $u(x,t) = \sum_{i=1}^{n} p_i(t) e^{-|x - q_i(t)|}$, where $p_i(t)$ and $q_i(t)$ are governed by $\frac{\partial q_i}{\partial t} = \sum_{i,j}^{n} p_j e^{-|q_i - q_j|}$ and $\frac{\partial p_i}{\partial t} = \sum_{i,j}^{n} p_i p_j\, sgn(q_i - q_j) e^{-|q_i - q_j|}$, respectively. Note that $n$ represents the number of peakons. This system of ordinary differential equations has the Hamiltonian pair given by $\dot{q}_i = \frac{\partial H}{\partial p_i}$ and $\dot{p}_i = -\frac{\partial H}{\partial q_i}$, where the Hamiltonian is $H(p,q) = \frac{1}{2}\sum_{i,j=1}^{n} p_i p_j e^{-|q_i - q_j|}$ [1]. Also, the CH equation can be expressed in a conservation law form as $\partial/\partial t(u - u_{xx}) + \partial/\partial x\left(\frac{3}{2}u^2 - \frac{1}{2}u_x^2 - uu_{xx}\right) = 0$.

The third-order derivative term and the mixed space–time derivative term in CH equation were less explored numerically in comparison with the first-order derivative term in CH equation and the pure spatial (or temporal) derivative terms. Hence, we intend to avoid these derivatives by transforming the third-order CH equation to its equivalent system of equations containing only the first-order spatial and temporal derivative terms. To this end, we will introduce one auxiliary variable later on. The resulting non-mixed space–time and first-order derivative terms can then be properly approximated by the numerical schemes developed in a stencil of fewer points. The key to success in predicting the resulting CH solution rests very much on how accurately the first-order derivative term is approximated. Hence the main focal point of this study is to minimize the dispersion error in the numerical approximation of the first-order derivative term. The other primary goal of the current study is to understand more about the interaction between the peakons and antipeakon.

The rest of this paper is organized as follows. Section 2 describes the nonlinear CH equation and reiterate some of its intriguing solution features. We then transform this equation, which contains the third-order derivative term, to its equivalent nonlinear system of equations with the reduced differential order and the inhomogeneous Helmholtz equation. In the first step of the proposed solution algorithm, the first-order nonlinear advection equation with the production term will be numerically approximated by the proposed combined compact finite difference scheme detailed in Section 4.2. We will then present in Section 5 the sixth-order accurate scheme for the Helmholtz equation. In Section 6, the problem with the smooth travelling solution will be solved at non-zero condition of $\kappa$ to justify the applicability of the proposed spatially fifth-order accurate upwind scheme to capture the dispersive travelling wave nature. In Section 7 the CH equation will be solved at four different initial conditions for showing how well the proposed symplecticity-preserving scheme with the minimal phase error can be applied to predict the transported peakons and antipeakon. The interaction details of the peakons and antipeakon will be explored by enlightening that the physical scenario after the peakon–antipeakon collision proceeds a total annihilation route. On the contrary, a total recovery (or switching) process will be revealed when the faster moving peakon takes

over the slower moving peakon without changing the conserved quantities. Finally, we will draw some concluding remarks in Section 8.

## 2. Working equation

In this paper the nonlinear partial differential equation (1), cast in the space–time independent variables $(x,t)$, is considered for modeling the time-evolving horizontal fluid velocity $u$ within the inviscid hydrodynamic context. The constant coefficient $\kappa$ in the equation is related to the critical shallow water wave speed [1]. Note that the solution $u(x,t)$ corresponds equivalently to the water's free surface for the two-dimensional shallow water wave over a flat bottom. Subsequent to the work of Fuchssteiner and Fokas [18], Camassa and Holm derived Eq. (1) by performing an asymptotic expansion on the Euler system of equations in terms of the aspect and amplitude ratios. Owing to the use of these two small expansion parameters, the derived CH equation falls into the weakly nonlinear and dispersive class of equations for the modeling of propagating water wave.

Besides the CH equation, the other two celebrated partial differential equations belonging to this weakly nonlinear and dispersive differential class are known as the Korteweg–de Vries (KdV), which models a small-amplitude long wave over the water surface in a channel, and the Benjamin–Bona–Mahony (BBM) equation, which was known as the regularized long-wave equation [19], were derived by means of the relative ordering instead of by exploiting the power law relation [20]. It is worthy to point out that Eq. (1) contains two other higher order derivative terms, owing to the use of a small amplitude expansion on the incompressible Euler's equation shown in the right-hand-side of CH equation, than those in the KdV and BBM equations [20]. Unlike the KdV and CH equations which possess the complete integrability property, BBM equation is not integrable and becomes therefore less attractive. The CH equation has the bi-Hamiltonian structure [18] and admits Lax pair of differential operators (or matrices) defined in the Hilbert space. In addition, CH equation permits smooth wave solution, traveling wave solution with the singularities of different kinds (peakon, cuspon, stumpon solutions), and infinitely many conserved integrals [1]. Note that peakon is a weak solution of the CH equation that may become non-smooth at some spatial points.

## 3. Two-step solution algorithm

The Camassa–Holm equation under current investigation is both nonlinear and dispersive. While CH equation has only one scalar variable, it contains many remarkable features for the cases investigated at different initial conditions. An initial solution can be evolved, for example, to form a wave of permanent form and, on the other hand, to a wave that can be broken in finite time. In case when wave breaks, the solution remains bounded while its derivative may be very large. The embedded bi-Hamiltonian structure and the theoretical existence of an infinite number of conservation laws result in the formal integrability of the equation [1]. In addition, at the peak of peakons the deterioration of smooth solution can lead to a high-frequency dispersive error when approximating the CH equation [6]. The complex dispersiveness present in such a non-smooth nonlinear system motivates us to develop a numerically stable and dispersively more accurate scheme for the investigated equation.

In the literature, much fewer numerical investigations of the Camassa–Holm equation have been made in comparison with the approximation of KdV equation. Camassa and Lee [20] reformulated Eq. (1) and introduced several "particles" along the characteristic curve of travelling wave throughout the physical domain. In particle method, the propagation solutions can be effectively calculated from the integral–differential system of nonlinear equations under different specified boundary conditions [20–23]. Two finite difference schemes proposed by Holden and Raynaud [24,25] contain the rigorous convergence proofs. A pseudospectral scheme developed by Kalisch and Lenells [26] was proven to be an effective means to predict the travelling wave solution from the CH equation. Both of the semi-discretized Fourier–Galerkin and Fourier-collocation methods are applicable to get a convergent CH solution [27]. Within the adaptive upwinding context, peakon solutions have been well predicted by Artebrant and Schroll [28] using the finite volume discretization method. The local discontinuous Galerkin method was also applied to solve the CH equation with success [6]. Other numerical methods, known as the multi-symplectic method [8], particle method [22–24], energy-conserving Galerkin method [29], self-adaptive mesh method [30] and minimized dispersion-error method [31], have also been proposed to solve the CH equation. To get a better predicted result for the soliton–cuspon or the cuspon–cuspon interaction problem, integrable discretizations of the soliton equation have been recently proposed. One can refer to [32] for additional details.

Since the investigated nonlinear equation (1) has the less familiar space–time mixed derivative term and third-order dispersive term, we intend to reformulate the CH equation and cast it to the equation having only the first-order derivatives. Two means can be chosen to reduce the differential order of the CH equation. One can rewrite (1) to the following first-order inhomogeneous linear equation

$$m_t + um_x + 2u_x m = -2\kappa u_x \tag{2}$$

The momentum variable given below is adopted in the so-called $u - m$ formulation of CH equation [31,33]

$$m = u - u_{xx} \tag{3}$$

One can also transform the original CH equation to its equivalent $u-P$ formulation. In the current study, the intermediate solution $u$ will be firstly computed from the following nonlinear convection equation, subject to the prescribed boundary conditions mentioned later in Sections 6 and 7 and the initial condition $u(x,t=0)=f\in H^1$:

$$u_t+uu_x=-P_x \tag{4}$$

The scalar variable $P$ in the $u-P$ formulation is governed by

$$P-P_{xx}=u^2+\frac{1}{2}u_x^2+2\kappa u \tag{5}$$

In the light of Eqs. (4), (5), we know that Eq. (1) is classified to be elliptic–hyperbolic provided that the CH solution remains smooth.

## 4. Discretization schemes

For approximating the time-dependent differential equation (4), in this study the classical semi-discretization method is adopted. We choose to approximate the time derivative terms before approximating the spatial derivative terms.

### 4.1. Symplectic time integration scheme

Since Eq. (1) has a multi-symplectic structure, the time-stepping scheme cannot be chosen arbitrarily. To get a long-term accurate solution, one should apply the symplectic structure-preserving numerical integrator to conserve symplecticity in the currently investigated Hamiltonian system. The sixth-order accurate symplectic Runge–Kutta scheme [34] is used in this study for performing a long-time integration of the CH equation:

$$u^{(1)}=u^n+\Delta t\left[\frac{5}{36}F^{(1)}+\left(\frac{2}{9}+\frac{2\tilde{c}}{3}\right)F^{(2)}+\left(\frac{5}{36}+\frac{\tilde{c}}{3}\right)F^{(3)}\right] \tag{6}$$

$$u^{(2)}=u^n+\Delta t\left[\left(\frac{5}{36}-\frac{5\tilde{c}}{12}\right)F^{(1)}+\left(\frac{2}{9}\right)F^{(2)}+\left(\frac{5}{36}+\frac{5\tilde{c}}{12}\right)F^{(3)}\right] \tag{7}$$

$$u^{(3)}=u^n+\Delta t\left[\left(\frac{5}{36}-\frac{\tilde{c}}{3}\right)F^{(1)}+\left(\frac{2}{9}-\frac{2\tilde{c}}{3}\right)F^{(2)}+\frac{5}{36}F^{(3)}\right] \tag{8}$$

$$u^{n+1}=u^n+\Delta t\left[\frac{5}{18}F^{(1)}+\frac{4}{9}F^{(2)}+\frac{5}{18}F^{(3)}\right] \tag{9}$$

where $\tilde{c}=\frac{1}{2}\sqrt{\frac{3}{5}}$ and $F^{(i)}=F(u^{(i)},\overline{P}^{(i)}),\ i=1,2,3$. In this applied symplectic Runge–Kutta method, in order to calculate $u^{n+1}$ from Eq. (9), we need to solve Eqs. (6)–(9) simultaneously (or implicitly) for obtaining $u^{(1)}$, $u^{(2)}$ and $u^{(3)}$. We then solve the Helmholtz equation (5) to get $\overline{P}^{(1)}$, $\overline{P}^{(2)}$ and $\overline{P}^{(3)}$. Upon reaching the convergence criteria, we can get the solution $u^{n+1}$ and then the solution $\overline{P}^{n+1}$. The above iterative processes will be repeated until the $L_2$-norm difference of two solutions calculated at consecutive iterations falls below the user's specified tolerance ($10^{-12}$ in the current study).

### 4.2. Combined compact scheme with minimized phase error

When solving the problem involving either a high wavenumber (or high frequency) or a small amplitude wave component, the number of grid points per wavelength required to resolve the shortest wave component becomes a practical consideration. We will therefore develop a combined compact finite difference scheme that has a higher-order accuracy and a better phase resolution in a stencil of fewer points. The first derivative term $\frac{\partial u}{\partial x}$ and the second derivative term $\frac{\partial^2 u}{\partial x^2}$ shown in Eq. (4) are approximated respectively by the following three-point combined compact finite difference scheme, which is developed in the mesh of uniform grid size $\Delta x=h$

$$a_1\left.\frac{\partial u}{\partial x}\right|_{i-1}+\left.\frac{\partial u}{\partial x}\right|_{i}=\frac{1}{h}(c_1u_{i-1}+c_2u_i+c_3u_{i+1})-h\left(b_1\left.\frac{\partial^2 u}{\partial x^2}\right|_{i-1}+b_2\left.\frac{\partial^2 u}{\partial x^2}\right|_{i}+b_3\left.\frac{\partial^2 u}{\partial x^2}\right|_{i+1}\right) \tag{10}$$

$$\bar{b}_1\left.\frac{\partial^2 u}{\partial x^2}\right|_{i-1}+\left.\frac{\partial^2 u}{\partial x^2}\right|_{i}+\bar{b}_3\left.\frac{\partial^2 u}{\partial x^2}\right|_{i+1}=\frac{1}{h^2}(\bar{c}_1u_{i-1}+\bar{c}_2u_i+\bar{c}_3u_{i+1})-\frac{1}{h}\left(\bar{a}_1\left.\frac{\partial u}{\partial x}\right|_{i-1}+\bar{a}_2\left.\frac{\partial u}{\partial x}\right|_{i}+\bar{a}_3\left.\frac{\partial u}{\partial x}\right|_{i+1}\right) \tag{11}$$

The above two combined compact schemes for $\left.\frac{\partial u}{\partial x}\right|_i$ and $\left.\frac{\partial^2 u}{\partial x^2}\right|_i$ are not independent of each other. They are rather strongly coupled through the terms $\left.\frac{\partial u}{\partial x}\right|_{i-1}$, $\left.\frac{\partial u}{\partial x}\right|_{i}$, $\left.\frac{\partial u}{\partial x}\right|_{i+1}$, $\left.\frac{\partial^2 u}{\partial x^2}\right|_{i-1}$, $\left.\frac{\partial^2 u}{\partial x^2}\right|_{i}$, $\left.\frac{\partial^2 u}{\partial x^2}\right|_{i+1}$, $u_{i-1}$, $u_i$ and $u_{i+1}$. For the sake of description, we consider the case involving only the positive-valued convective coefficient. The scheme for the case with negative convective coefficient can be similarly derived.

*4.2.1. Combined compact scheme for the second-order derivative term*

We will approximate $\frac{\partial^2 u}{\partial x^2}$ by a center scheme owing to its dissipative nature. To get a higher spatial accuracy, the weighting coefficients shown in Eq. (11) can be, as a result, determined solely from the modified equation analysis. Derivation of the coefficients $\bar{a}_1,\ \bar{a}_2,\ \bar{a}_3,\ \bar{b}_1,\ \bar{b}_3,\ \bar{c}_1,\ \bar{c}_2$ and $\bar{c}_3$ starts by performing the Taylor series expansions on the terms $u_{i\pm1}$, $\left.\frac{\partial u}{\partial x}\right|_{i\pm1}$ and $\left.\frac{\partial^2 u}{\partial x^2}\right|_{i\pm1}$ with respect to $u_i$, $\left.\frac{\partial u}{\partial x}\right|_i$ and $\left.\frac{\partial^2 u}{\partial x^2}\right|_i$ and, then, eliminating the leading error terms derived in the modified equation. We can then derive the coefficients in Eq. (11) as $\bar{a}_1=-\frac{9}{8},\ \bar{a}_2=0,\ \bar{a}_3=\frac{9}{8},\ \bar{b}_1=-\frac{1}{8},\ \bar{b}_3=-\frac{1}{8},\ \bar{c}_1=3,\ \bar{c}_2=-6$ and $\bar{c}_3=3$ [35]. In view of the following derived modified equation, employment of this set of coefficients renders the approximated $\frac{\partial^2 u}{\partial x^2}$ with the spatial accuracy order of sixth

$$\frac{\partial^2 u}{\partial x^2}=\left.\frac{\partial^2 u}{\partial x^2}\right|_{exact}+\frac{h^6}{20,160}\frac{\partial^8 u}{\partial x^8}+\frac{h^8}{604,800}\frac{\partial^{10} u}{\partial x^{10}}+O(h^{12})+\cdots$$

*4.2.2. Optimized combined compact scheme for the first-order derivative term*

In this study we will combine the traditional truncated Taylor series analysis with the Fourier analysis proposed in the work of Tam and Webb [36] to develop a scheme with better dispersive resolution. Following this line of thought, the coefficients $a_1, b_1, b_2, b_3, c_1, c_2$ and $c_3$ are partly determined by performing Taylor series expansions on $u_{i\pm1}$, $\left.\frac{\partial u}{\partial x}\right|_{i-1}$ and $\left.\frac{\partial^2 u}{\partial x^2}\right|_{i\pm1}$ with respect to $u_i$, $\left.\frac{\partial u}{\partial x}\right|_i$ and $\left.\frac{\partial^2 u}{\partial x^2}\right|_i$, respectively. By eliminating the leading six discretization error terms derived in the modified equation, the following set of six algebraic equations for Eq. (10) can be derived as

$$c_1+c_2+c_3=0 \tag{12}$$

$$-a_1-c_1+c_3=1 \tag{13}$$

$$-a_1+b_1+b_2+b_3-\frac{c_1}{2}-\frac{c_3}{2}=0 \tag{14}$$

$$\frac{a_1}{2}-b_1+b_3+\frac{c_1}{6}-\frac{c_3}{6}=0 \tag{15}$$

$$-\frac{a_1}{6}+\frac{b_1}{2}+\frac{b_3}{2}-\frac{c_1}{24}-\frac{c_3}{24}=0 \tag{16}$$

$$\frac{a_1}{24}-\frac{b_1}{6}+\frac{b_3}{6}+\frac{c_1}{120}-\frac{c_3}{120}=0 \tag{17}$$

After performing the above modified equation analysis, we will adopt the minimization method described below to get the seventh algebraic equation in the wavenumber space.

Since the equation under current investigation permits a wave-like solution, application of the modified equation analysis (or truncation error analysis) is not enough to get all the characteristics in the CH solution. As a result, we need to reduce another type of errors instead of reducing only the truncation error. In this study we adopt the Fourier analysis method to provide some additional information about the resolution characteristics. In Fourier analysis, we demand that the Fourier transform of the partial derivative terms on the right hand side of (10) is a close approximation to that of the partial derivatives on the left hand side. Since Fourier transform is involved in the development of the following optimized spatial discretization scheme, we define the Fourier transform and its inverse for $u$ given below

$$\tilde{u}(\alpha)=\frac{1}{2\pi}\int_{-\infty}^{+\infty}u(x)\exp(-\mathbf{i}\alpha x)dx, \tag{18}$$

$$u(x)=\int_{-\infty}^{+\infty}\tilde{u}(\alpha)\exp(\mathbf{i}\alpha x)d\alpha \tag{19}$$

where $\mathbf{i}$ is equal to $\sqrt{-1}$. Development of the approximation scheme for $\frac{\partial u}{\partial x}$ is followed by performing Fourier transform on each term shown in Eqs. (10) and (11). The expressions of the wavenumber $\alpha$ for these two equations can be therefore derived as

$$\mathbf{i}\alpha h(a_1\exp(-\mathbf{i}\alpha h)+1)\simeq c_1\exp(-\mathbf{i}\alpha h)+c_2+c_3\exp(\mathbf{i}\alpha h)-(\mathbf{i}\alpha h)^2(b_1\exp(-\mathbf{i}\alpha h)+b_2+b_3\exp(\mathbf{i}\alpha h)) \tag{20}$$

$$(\mathbf{i}\alpha h)^2\left(-\frac{1}{8}\exp(-\mathbf{i}\alpha h)+1-\frac{1}{8}\exp(\mathbf{i}\alpha h)\right)\simeq 3\exp(-\mathbf{i}\alpha h)-6+3\exp(\mathbf{i}\alpha h)-\mathbf{i}\alpha h\left(-\frac{8}{9}\exp(-\mathbf{i}\alpha h)+\frac{8}{9}\exp(\mathbf{i}\alpha h)\right) \tag{21}$$

To get the same expressions as those shown in the right-hand sides of Eqs. (20) and (21), we express the numerical (or effective) wavenumbers $\alpha'$ and $\alpha''$ as follows [36]:

$$\mathbf{i}\alpha' h(a_1\exp(-\mathbf{i}\alpha h)+1)=c_1\exp(-\mathbf{i}\alpha h)+c_2+c_3\exp(\mathbf{i}\alpha h)-(\mathbf{i}\alpha'' h)^2(b_1\exp(-\mathbf{i}\alpha h)+b_2+b_3\exp(\mathbf{i}\alpha h)) \tag{22}$$

$$\mathbf{i}\alpha' h\left(-\frac{8}{9}\exp(-\mathbf{i}\alpha h)+\frac{8}{9}\exp(\mathbf{i}\alpha h)\right)=3\exp(-\mathbf{i}\alpha h)-6+3\exp(\mathbf{i}\alpha h)-(\mathbf{i}\alpha'' h)^2\left(-\frac{1}{8}\exp(-\mathbf{i}\alpha h)+1-\frac{1}{8}\exp(\mathbf{i}\alpha h)\right) \tag{23}$$

By solving Eqs. (22) and (23), we get the following two expressions for $\alpha'$ and $\alpha''$

$$\begin{aligned}\alpha' h = & -\mathbf{i}(24b_1\exp(-2\mathbf{i}\alpha h)+c_1\exp(-2\mathbf{i}\alpha h)+c_3+c1+24b_1+c_2\exp(-\mathbf{i}\alpha h)+24b_2\exp(-\mathbf{i}\alpha h)\\ & +24b_3-48b_1\exp(-\mathbf{i}\alpha h)-8c_1\exp(-\mathbf{i}\alpha h)-48b_3\exp(\mathbf{i}\alpha h)+24b_2\exp(\mathbf{i}\alpha h)+24b_3\exp(2\mathbf{i}\alpha h)-48b_2\\ & +c_2\exp(\mathbf{i}\alpha h)+c_3\exp(2\mathbf{i}\alpha h)-8c_3\exp(\mathbf{i}\alpha h)-8c_2)/(-8+\exp(\mathbf{i}\alpha h)-8a_1\exp(-\mathbf{i}\alpha h)+a_1\exp(-2\mathbf{i}\alpha h)\\ & -9b_1\exp(-2\mathbf{i}\alpha h)-9b_2\exp(-\mathbf{i}\alpha h)+9b_2\exp(\mathbf{i}\alpha h)+9b_3\exp(2\mathbf{i}\alpha h)+a_1+9b_1-9b_3+\exp(\mathbf{i}\alpha h))\end{aligned} \tag{24}$$

$$\alpha'' h=\sqrt{-\frac{3\exp(-\mathbf{i}\alpha h)-6+3\exp(\mathbf{i}\alpha h)-\mathbf{i}\alpha' h\left(-\frac{8}{9}\exp(-\mathbf{i}\alpha h)+\frac{8}{9}\exp(\mathbf{i}\alpha h)\right)}{-\frac{1}{8}\exp(-\mathbf{i}\alpha h)+1-\frac{1}{8}\exp(\mathbf{i}\alpha h)}} \tag{25}$$

Note that the real part $\Re[\alpha' h]$ and the imaginary part $\Im[\alpha' h]$ of the modified (or scaled) wavenumber $\alpha' h$ are associated respectively with the dispersion (or phase) error and the dissipation (or amplitude) error [33]. The above Fourier transform analysis performed on the combined compact finite-difference equations gives us a good approximation to the CH equation as $\alpha h$ is equal to the real part of $\alpha'\ h$. This implies that the function $E(\alpha)$ defined below should be a very small and positive magnitude within a particular wavenumber range

$$E(\alpha)=\int_{-\frac{\pi}{2}}^{\frac{\pi}{2}}[W(\alpha h-\Re[\alpha' h])]^2 d(\alpha h)=\int_{-\frac{\pi}{2}}^{\frac{\pi}{2}}[W(\gamma-\Re[\gamma'])]^2 d\gamma \tag{26}$$

In the above, $\gamma = \alpha h$ and $\gamma' = \alpha'\ h$. Note that Eq. (26) can be analytically integrated provided that the weighting function $W$ is chosen as the denominator of $(\gamma-\Re[\gamma'])$, which is

$$\begin{aligned}W= & -16+72b_3+72b_1-81b_1^2-81b_3^2-81b_2^2-162b_2b_3\cos(\gamma)-144a_1b_3\cos(\gamma)-162b_1b_2\cos(\gamma)-a_1^2\cos(\gamma)^2\\ & +8a_1^2\cos(\gamma)-18b_3\cos(\gamma)^3+18b_1\cos(\gamma)^3+81b_2^2\cos(\gamma)^2+162b_1b_3-72b_1\cos(\gamma)^2+81b_3^2\cos(\gamma)^2+81b_1^2\cos(\gamma)^2\\ & -72a_1b_2-18b_1\cos(\gamma)+16a_1\cos(\gamma)^2-2a_1\cos(\gamma)^3+72b_3\cos(\gamma)^2+18b_3\cos(\gamma)-32a_1\cos(\gamma)-36a_1b_3\cos(\gamma)^4\\ & -18a_1b_2\cos(\gamma)^3+162b_2b_3\cos(\gamma)^3+162b_1b_2\cos(\gamma)^3+324b_1b_3\cos(\gamma)^4+72a_1b_2\cos(\gamma)^2+144a_1b_3\cos(\gamma)^3\\ & -486b_1b_3\cos(\gamma)^2+36a_1b_3\cos(\gamma)^2+18a_1b_2\cos(\gamma)+8\cos(\gamma)-16a_1^2-\cos(\gamma)^2\end{aligned} \tag{27}$$

To give a good approximation to the derivative terms, the numerical modified (or scaled) wavenumber should match well with its corresponding exact modified wavenumber. Since $\alpha h$ is not necessarily equal to $\Re[\alpha' h]$, numerical dispersion error will be produced. In this study we maximize the dispersion accuracy by minimizing the integrated error function $E(\alpha)$ shown in (26). Instead of imposing the extreme conditions $\frac{\partial E}{\partial a_1}=\frac{\partial E}{\partial c_1}=\frac{\partial E}{\partial c_2}=\frac{\partial E}{\partial c_3}=\frac{\partial E}{\partial b_1}=\frac{\partial E}{\partial b_2}=\frac{\partial E}{\partial b_3}=0$ to get all the algebraic equations for determining the weighting coefficients by making $E$ a minimum, we adopt here the constrained minimization approach to minimize the integrated error function $E$. To make $E$ defined in Eq. (26) to be positive and minimal the following extreme condition is enforced on the free parameter $c_3$

$$\frac{\partial E}{\partial c_3}=0 \tag{28}$$

The above equation, which is enforced to optimize the spatial discretization scheme, will be used together with the other six algebraic equations which are derived previously by way of the modified equation analysis to reduce the dissipation error as well as to get a higher dispersion accuracy. The resulting seven introduced coefficients given below can be uniquely determined as

$$a_1=0.875 \tag{29}$$
$$b_1=0.12512823 \tag{30}$$
$$b_2=-0.24871766 \tag{31}$$
$$b_3=0.00012823 \tag{32}$$
$$c_1=-1.93596119 \tag{33}$$
$$c_2=1.99692238 \tag{34}$$
$$c_3=-0.06096119 \tag{35}$$

Based on the modified equation derived below, we know that the proposed upwinding scheme for $\frac{\partial\phi}{\partial x}$ has the spatial accuracy order of fifth

$$\frac{\partial\phi}{\partial x}=\frac{\partial\phi}{\partial x}\bigg|_{exact}-0.00070086h^5\frac{\partial^6\phi}{\partial x^6}+0.00019841h^6\frac{\partial^7\phi}{\partial x^7}-0.00004988h^7\frac{\partial^8\phi}{\partial x^8}+O(h^8)+\cdots \tag{36}$$

For the approximation of the gradient term $P_x$, we apply the central-type CCD scheme proposed by Chu and Fan [35].

## 5. Three-point sixth-order accurate compact Helmholtz scheme for $P$

In order to develop a higher-order numerical method for the Helmholtz equation, one can always introduce more grid points in the computational stencil. The solution accuracy is improved, however, at the cost of an expensive matrix calculation. For developing an efficient and accurate numerical scheme, we propose the following sixth-order accurate compact scheme in a three-point stencil.

The following prototype equation with $f\ (\equiv -u^2 - \frac{1}{2}u_x^2 - 2ku)$ will be considered

$$\frac{\partial^2 P}{\partial x^2} - kP = f(x). \tag{37}$$

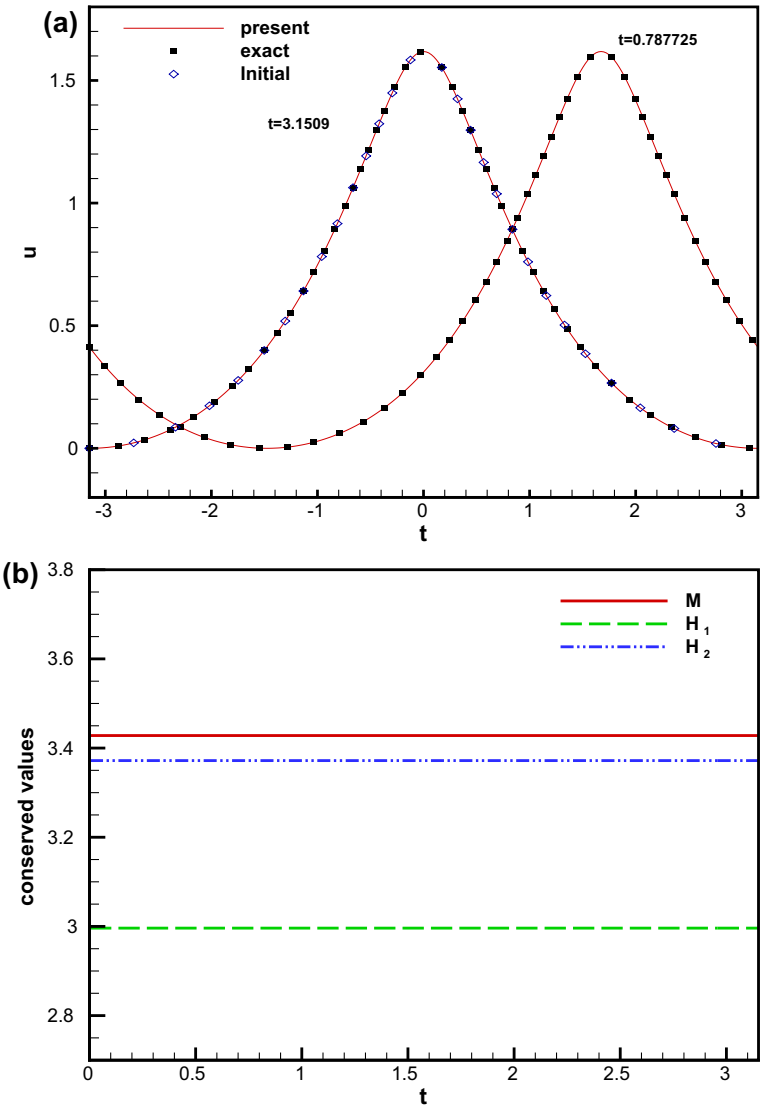


**Fig. 1.** Verification of the predicted solution for the test problem given in Section 6. (a) comparison of the predicted and exact traveling wave solutions over one period of time $0 \leqslant t \leqslant 3.1509$; (b) plot of the conserved quantities $M = \int_{-\infty}^{+\infty} u\,dx$; $H_1 = \frac{1}{2}\int_{-\infty}^{+\infty}(u^2 + u_x^2)dx$ and $H_2 = \frac{1}{2}\int_{-\infty}^{+\infty}(u^3 + uu_x^2 + 2\kappa u^2)dx$ against time.

**Table 1**
The predicted spatial rates of convergence for the test problem given in Section 6. Note that the time increment $\Delta t = 0.49233 \times 10^{-3}$ is much smaller than the grid size $\Delta x = \frac{6.3019}{128}$.

| $N$ | 32 | 64 | 128 |
|---|---|---|---|
| $L_2$-error norm | 1.939E−3 | 3.962E−5 | 9.330E−7 |
| rate of convergence | – | 5.613 | 5.408 |

We denote the values of $\partial^2 P/\partial x^2$, $\partial^4 P/\partial x^4$ and $\partial^6 P/\partial x^6$ at a nodal point $i$ as

$$\left.\frac{\partial^2 P}{\partial x^2}\right|_i = s_i \tag{38}$$

$$\left.\frac{\partial^4 P}{\partial x^4}\right|_i = v_i \tag{39}$$

$$\left.\frac{\partial^6 P}{\partial x^6}\right|_i = w_i \tag{40}$$

Development of the compact scheme for (37) at the point $i$ starts with relating the derivative terms $v$, $s$ and $w$ with $P$ by means of the equation given below

$$\delta_0 h^6 w_i + \gamma_0 h^4 v_i + \beta_0 h^2 s_i = \alpha_1 P_{i+1} + \alpha_0 P_i + \alpha_{-1} P_{i-1}. \tag{41}$$

It is legitimate to set $\alpha_1 = \alpha_{-1}$ because of the elliptic nature of the Helmholtz equation (or Eq. (37)). Having set $\alpha_1 = \alpha_{-1}$, we expand $P_{i\pm1}$ with respect to $P_i$ in Taylor series. After the substitution of these expansion equations into Eq. (41), we can get

$$\delta_0 h^6 w_i + \gamma_0 h^4 v_i + \beta_0 h^2 s_i = (\alpha_0 + 2\alpha_1) P_i + 2\alpha_1 \left[\frac{h^2}{2!}\frac{\partial^2 P_i}{\partial x^2} + \frac{h^4}{4!}\frac{\partial^4 P_i}{\partial x^4} + \frac{h^6}{6!}\frac{\partial^6 P_i}{\partial x^6} + \frac{h^8}{8!}\frac{\partial^8 P_i}{\partial x^8} + \cdots\right] \tag{42}$$

Through a term-by-term comparison of the derivative terms shown in Eq. (42), a set of five algebraic equations can be derived. Hence, the introduced free parameters can be determined as $\alpha_1 = \alpha_{-1} = -1$, $\alpha_0 = 2$, $\beta_0 = -1$, $\gamma_0 = -\frac{1}{12}$ and $\delta_0 = -\frac{1}{360}$. Since $w_i = k^3 P_i + k^2 f_i + k\frac{\partial^2 f_i}{\partial x^2} + \frac{\partial^4 f_i}{\partial x^4}$, $v_i = k^2 P_i + k f_i + \frac{\partial^2 f_i}{\partial x^2}$ and $s_i = k P_i + f_i$, Eq. (41) can then be further expressed as

$$\alpha_1 P_{i+1} + \left(\alpha_0 - \beta_0 h^2 k - \gamma_0 h^4 k^2 - \delta_0 h^6 k^3\right) P_i + \alpha_1 P_{i-1} = \left[h^2 \beta_0 f_i + h^4 \gamma_0 \left(k f_i + \frac{\partial^2 f_i}{\partial x^2}\right) + h^6 \delta_0 \left(k^2 f_i + k\frac{\partial^2 f_i}{\partial x^2} + \frac{\partial^4 f_i}{\partial x^4}\right)\right] \tag{43}$$

or

$$P_{i+1} - \left(2 + h^2 k + \frac{1}{12} h^4 k^2 + \frac{1}{360} h^6 k^3\right) P_i + P_{i-1} = h^2 f_i + \frac{1}{12} h^4 \left(k f_i + \frac{\partial^2 f_i}{\partial x^2}\right) + \frac{1}{360} h^6 \left(k^2 f_i + k\frac{\partial^2 f_i}{\partial x^2} + \frac{\partial^4 f_i}{\partial x^4}\right) \tag{44}$$

The corresponding modified equation for (37) shown below confirms that the proposed three-point stencil compact scheme is indeed sixth-order accurate

$$\frac{\partial^2 P}{\partial x^2} - kP = f + \frac{h^6}{20,160}\frac{\partial^8 P}{\partial x^8} + \frac{h^8}{1,814,400}\frac{\partial^{10} P}{\partial x^{10}} + \cdots + H.O.T. \tag{45}$$

## 6. Verification studies

To begin with, the analytic problem admitting a periodic travelling wave solution $u(x,t) = U(x - ct)$ is chosen to justify the integrity of the developed scheme for solving the nonlinear CH equation [20]

$$U' = \pm\sqrt{\frac{-U^3 + (c - 2\kappa)U^2 + C(A)U}{c - U}} \tag{46}$$

**Table 2**
The predicted temporal rates of convergence for the test problem given in Section 6 with $N = 128$ nodal points.

| $\Delta t$ | 1.125E−1 | 1.086E−1 | 1.050E−1 |
|---|---|---|---|
| $L_2$-error norm | 4.115E−05 | 3.404E−05 | 2.833E−05 |
| Rate of convergence | – | 5.400 | 5.413 |

**Table 3**
The predicted spatial rates of convergence for the problem given in Section 6 based on the solutions calculated at the fixed value of $c\frac{\Delta t}{\Delta x} = 1/4$.

| Number of nodal points | $L_2$-error norm | | Rate of convergence | |
|---|---|---|---|---|
| | $u - P$ formulation | $u - m$ formulation | $u - P$ formulation | $u - m$ formulation |
| $N = 32$ | 1.939E−3 | 6.446E−3 | – | – |
| $N = 64$ | 3.962E−5 | 1.498E−4 | 5.613 | 5.426 |
| $N = 128$ | 9.330E−7 | 3.635E−6 | 5.408 | 5.365 |

Note that $A$ and $U$ are implicitly related to the independent variable $x$ by $x = \frac{2}{\sqrt{a_1(a_2-a_3)}}(a_1 - a_2)\Pi$, where $\Pi$ is the elliptic function, $a_1 = c,\ a_2 = \frac{1}{2}(c - 2\kappa + \sqrt{(c-2\kappa)^2 + 4C})$ and $a_3 = \frac{1}{2}(c - 2\kappa - \sqrt{(c-2\kappa)^2 + 4C})$.

Calculation will be carried out at $c = 2$, $\kappa = 1/2$ and $C = 1$ in this validation study. The time step, which is $\Delta t = \frac{1}{4}\Delta x$, and the grid size, which is $\Delta x = 0.0492$ (or 128 nodal points), are chosen. The waveform predicted at $t = 0.787725$ will be plotted together with the exact solution and the initial traveling wave solution marked by the dot-dash line. After one time period, the predicted waveform shown in Fig. 1(a) matches well with the initial waveform. The values of $M = \int_{-\infty}^{+\infty} u\,dx$, $H_1 = \frac{1}{2}\int_{-\infty}^{+\infty}(u^2 + u_x^2)dx$ and $H_2 = \frac{1}{2}\int_{-\infty}^{+\infty}(u^3 + uu_x^2 + 2\kappa u^2)dx$ are also calculated against time. It can be clearly seen from Fig. 1(b) that these values indeed remain unchanged as the initial values of 3.428, 2.996 and 3.372 for $M$, $H_1$ and $H_2$, respectively.

For the sake of completeness, the computed results in association with the grid and time refinements are tabulated respectively in Tables 1 and 2. Note that the spatial rates of convergence are computed from the $L_2$ error norms. The spatial and temporal rates of convergence shown in Tables 1 and 2 are approximately equal to 5.5 and 5.4, respectively. These computed rates are satisfactory since the employed scheme is fifth-order accurate for the advection term and is sixth-order accurate for the rest of spatial derivative terms while the time-stepping scheme is sixth-order accurate.

We also assess the $u - P$ and $u - m$ formulations in terms of the predicted accuracy. Based on the computed results tabulated in Table 3, one can see that the proposed $u - P$ formulation gives more accurate results in comparison with those predicted from the $u - m$ formulation. This confirms the applicability of the presently employed $u - P$ formulation to carry out the rest of numerical studies.

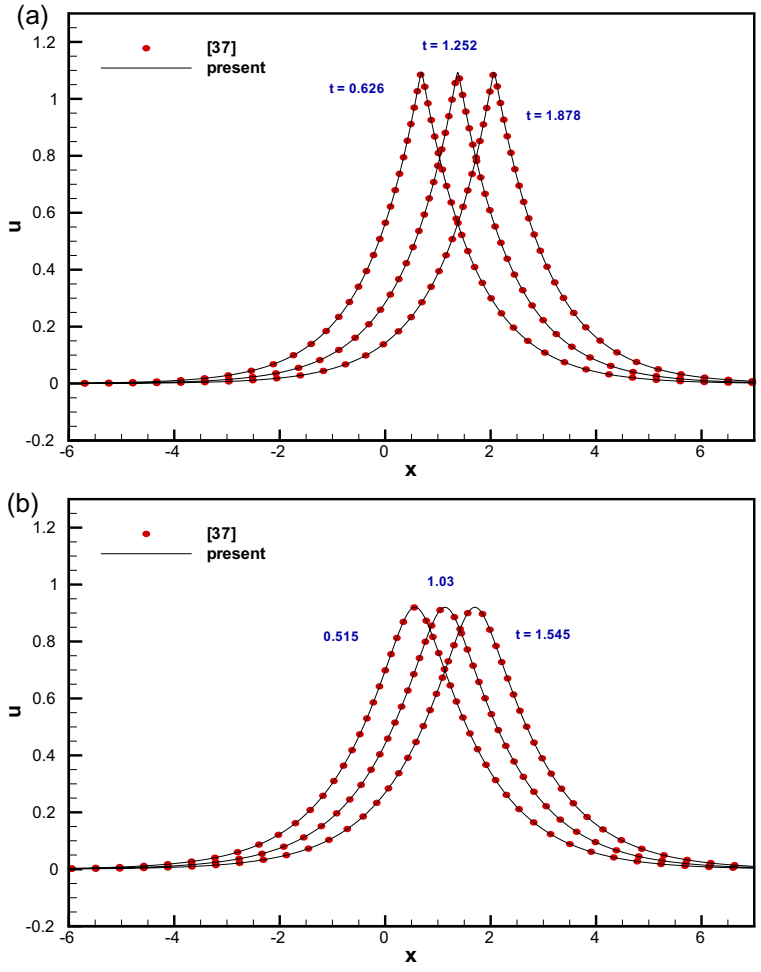


**Fig. 2.** Comparsion of the predicted time-varying one-soliton solutions ($\kappa = 0.0036$ in (a)) and ($\kappa = 0.09$ in (b)) computed form the proposed scheme in 16,384 mesh points and the *PQ*-decomposition scheme [37] at three different times.

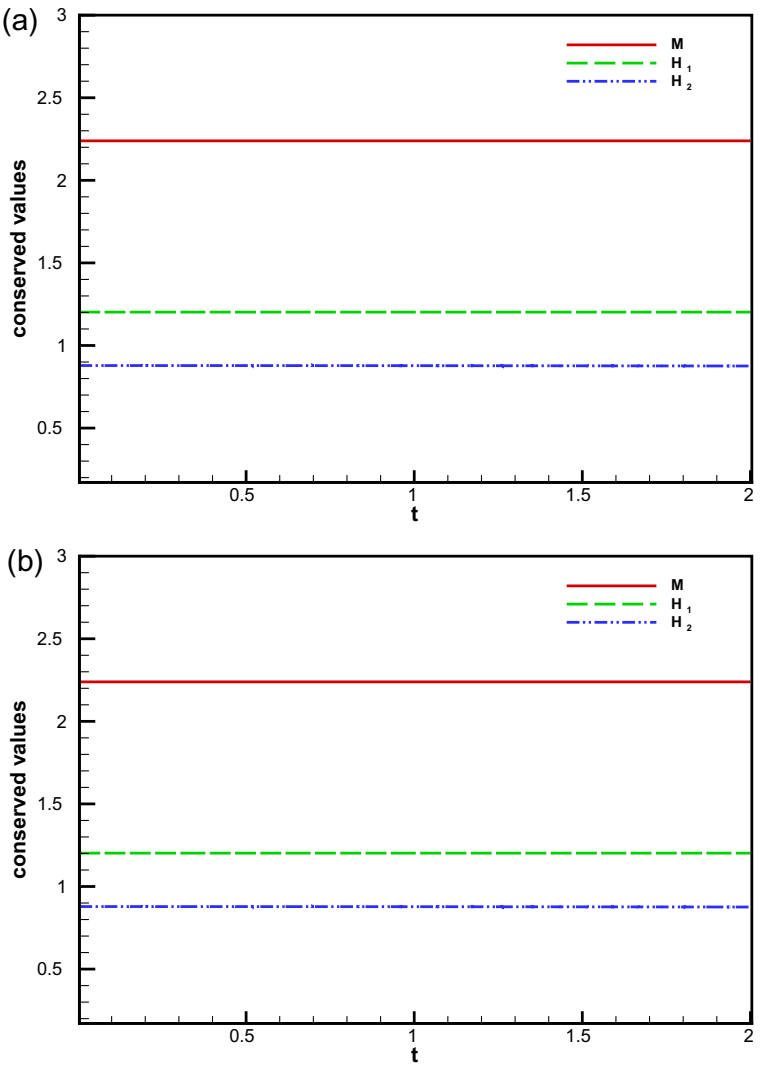


**Fig. 3.** Plot of the computed values of $M = \int_{-\infty}^{+\infty} u\,dx$, $H_1 = \frac{1}{2}\int_{-\infty}^{+\infty}(u^2 + u_x^2)dx$ and $H_2 = \frac{1}{2}\int_{-\infty}^{+\infty}(u^3 + uu_x^2 + 2\kappa u^2)dx$ against time for the investigated one-soliton problem. (a) $\kappa = 0.0036$; (b) $\kappa = 0.09$.

Based on the $u - P$ formulation, we then solve Eq. (1) at $\kappa = 0.0036$ and $\kappa = 0.09$ for the one-soliton case that was considered previously in [37]. The results computed in a domain of 16,384 uniform mesh points will be compared with the results computed from the method of *PQ*-decomposition [37]. Fig. 2(a) and (b) shows good agreement between the two results that are plotted at the three chosen times. For the sake of validation, we also plot the values of $M_1$,$H_1$ and $H_2$ for the cases investigated at $\kappa = 0.0036$ and $\kappa = 0.09$ against time. One can clearly see from Fig. 3 that the predicted Hamiltonians remain almost unchanged. The proposed CH scheme is validated.

## 7. Peakon and/or antipeakon interaction problems

The Camassa–Holm equation admits the peakon, cuspon and stumpon solutions [38]. Peakon (or a peaked solitary wave) is a soliton with finite-valued discontinuous first derivative. This travelling wave solution can be algebraically expressed by $\phi(x,t) = ce^{-|x-ct|}$, where $c$ represents the wave amplitude and speed. If $c$ is negative, the wave propagates leftwards with its peak pointing downwards. Such a peaked solution is sometimes called as an antipeakon. Cuspon also involves discontinuous first derivative. In contrast to the peakon solution, the slopes of cuspon at the locations immediately adjacent to the point with the discontinuous first derivative are both infinitely large [39].

The solutions for the Camassa–Holm equation can be divided into two mutually exclusive classes. One class of the CH solutions is globally smooth in time. The other class of the wave breaking solutions, which is Hölder continuous and uniformly bounded, will develop an unbounded slope in finite time [40].

The Camassa–Holm equation is known to be amenable to the multipeakon solutions. For the multi-peakon cases with $n$ (=2,3,4), we intend to clarify whether the solution $u(x,t>0)$ remains to be globally smooth or will be gradually evolved to exhibit a breaking wave pattern in finite time. We aim, in particular, to gain some insights into the peakon/antipeakon interaction after wave breaking.

### 7.1. Peakon–peakon interaction problem

We consider firstly the case with the two peakons propagating along the same direction [37]. The following initial data for Eq. (1) investigated at $\kappa = 0$ is specified in the domain $-60 \leqslant x \leqslant 60$

$$u_0(x, t = -20) = p_1(t)e^{-|x-q_1(t)|} + p_2(t)e^{-|x-q_2(t)|} \tag{47}$$

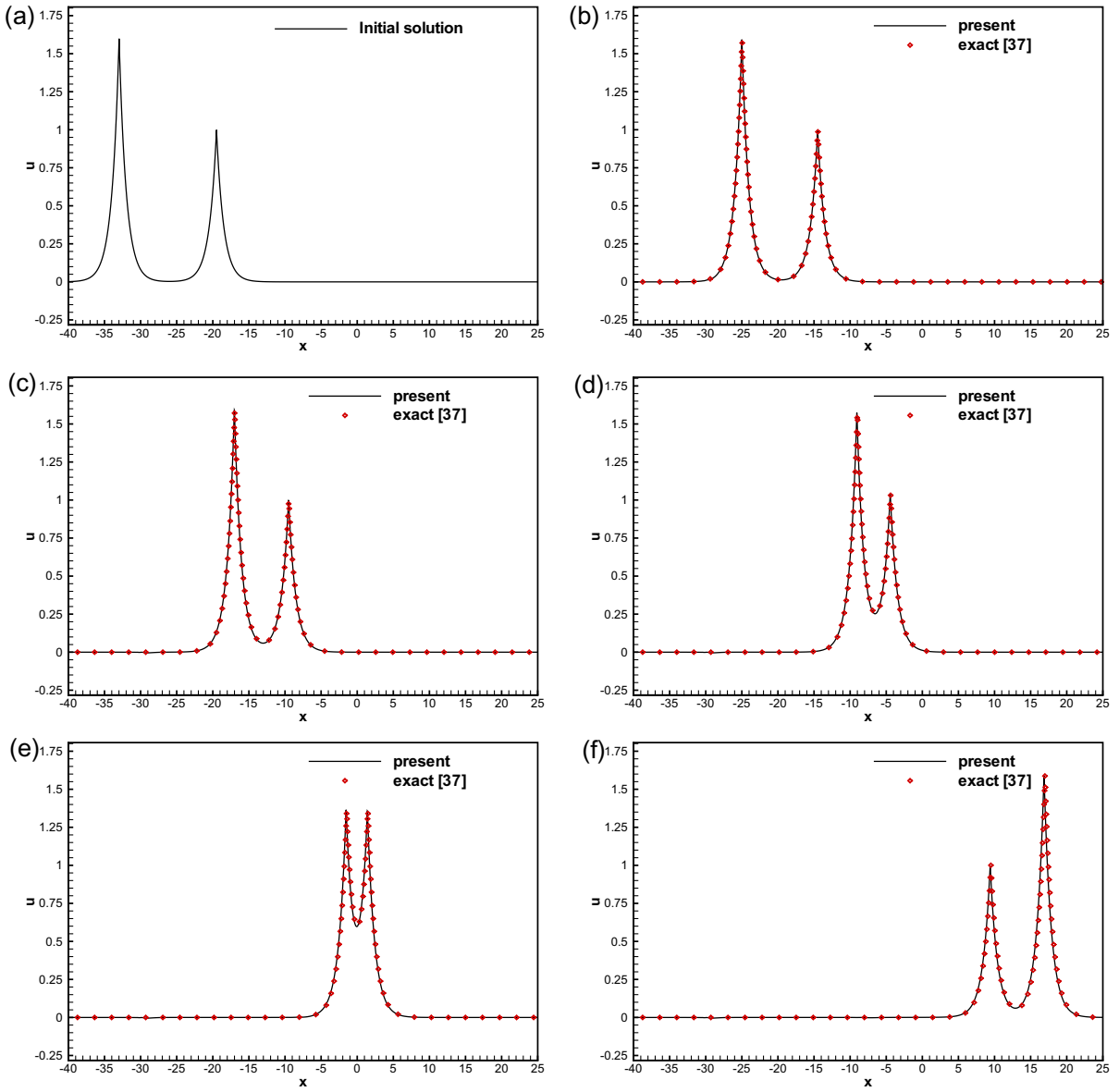


**Fig. 4.** Comparison of the predicted and exact [37] peakon–peakon solutions computed in 16,384 grids at different times. (a) $t = -20.0$; (b) $t = -15.0$; (c) $t = -10.0$; (d) $t = -5.0$; (e) $t = 0.0$; (e) $t = 10.0$.

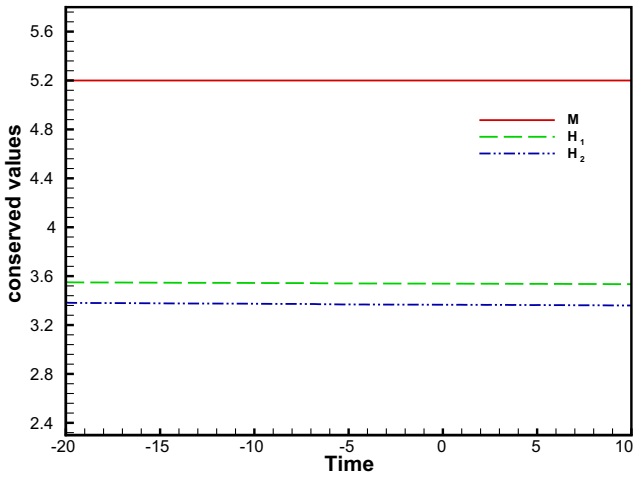


**Fig. 5.** Plot of the values of $M = \int_{-\infty}^{+\infty} u\,dx$ and two Hamiltonians $H_1 = \frac{1}{2}\int_{-\infty}^{+\infty}(u^2 + u_x^2)dx$ and $H_2 = \frac{1}{2}\int_{-\infty}^{+\infty}(u^3 + uu_x^2 + 2\kappa u^2)dx$ against time for the investigated peakon–peakon problem.

In this case, two peakons move towards the $x$-direction with $p_1(t) = \frac{c_2E_1 + c_1E_2}{E_1 + E_2}$ and $p_2(t) = \frac{c_1E_1 + c_2E_2}{E_1 + E_2}$, where $E_i(t) = e^{c_i t}$ $(i = 1,2)$ with $c_1 = 1.6$ and $c_2 = 1.0$. The Camassa–Holm equation will be solved at $q_1(t) = \ln\left[\frac{(c_1 - c_2)E_1E_2}{c_2E_1 + c_1E_2}\right]$ and $q_2(t) = \ln\left[\frac{c_1E_1 + c_2E_2}{c_1 - c_2}\right]$ in a domain with the periodic boundary conditions.

In Fig. 4, the time-evolving two-peakon solutions, predicted in a domain of 16,384 uniformly discretized grids, compare excellently with the exact results given in [37]. Switching scenario is clearly confirmed in the sense that the two investigated peakon waves pass through each other and they remain still as the solitary waves. Since no wave breaking has been observed, we know that this two-peakon problem has a global solution. In addition, the higher peakon was seen to move faster than the lower one. At the time $t = 0.0$ the higher peakon overtakes the lower peakon with the accompanied exchange of the value $\int u\,dxd$. While exchange of the individual value of $M$ indeed exists between the two right-running individual peakons, the total values of $M$, $H_1$ and $H_2$ shown in Fig. 5 are unchanged all the time.

### 7.2. One-peakon and one-antipeakon interaction problem

The next peakon–antipeakon interaction problem, subject to the following initial profile, will be studied in the domain $-20 \leqslant x \leqslant 20$

$$u(x, t = 0) = p_1(t)e^{-|x - q_1(t)|} + p_2(t)e^{-|x - q_2(t)|} \tag{48}$$

In the above, we specify $q_1 = \ln\left(\frac{c_1 - c_2}{c_1e^{-c_1(t-\tau)} - c_2e^{-c_2(t-\tau)}}\right)$, $q_2 = \ln\left(\frac{c_1e^{c_1(t-\tau)} - c_2e^{c_2(t-\tau)}}{c_1 - c_2}\right)$, $p_1 = \frac{c_1^2 - c_2^2e^{(c_1 - c_2)(t-\tau)}}{c_1 - c_2e^{(c_1 - c_2)(t-\tau)}}$, and $p_2 = \frac{c_1^2 - c_1^2e^{(c_1 - c_2)(t-\tau)}}{c_2 - c_1e^{(c_1 - c_2)(t-\tau)}}$, $c_1 = 10$, $c_2 = -5$ and $\tau = 1$. Subject to the periodic boundary condition, CH equation will be solved in the domain of 32,768 uniform grids.

In Fig. 6(a), one peakon initially moves to the right and the other antipeakon moves to the left. The computed time-evolving solutions plotted in Fig. 6 compare well with the results in [41]. One can find from the predicted solution that the antipeakon disappears pointwise after the collision time at $t = 0.95$. The total annihilation scenario is, thus, exhibited after the head-on collision. Such a dissipative phenomenon has been observed and discussed in [40,42]. For the validation purpose we plot the locations of peakon and antipeakon before the collision time and the peakon location after the time of head-on collision. Good agreement between two solutions can be seen in Fig. 7.

The values of $M$, $H_1$ and $H_2$ plotted in Fig. 8 remain unchanged prior to the collision time at $t = 0.95$. Such a numerically predicted conservation phenomenon is under our expectation since the Camassa–Holm equation satisfies the least action Principle [15,11]. At a time after the peakon/antipeakon collision, the peakon and antipeakon pass through each other in a way that the total value of $H_1$ is no longer conserved. Two components in the Hamiltonian $H_1$, which are $\int_{-\infty}^{\infty} u^2\,dx$ and $\int u_x^2\,dx$, are plotted against time to examine which one has caused the value of $H_1$ to decrease after the time of peakon–antipeakon collision. In Fig. 9 we clearly observe a rapid decrease of the value $\int_{-\infty}^{\infty} u_x^2\,dx$ at a time of peakon/antipeakon collision. While $M$ remains unchanged, the predicted value of $H_1$ decreases sharply at the time when the peakon collides with the antipeakon. The solution of this head-on peakon/antipeakon interaction problem is globally dissipative in the sense that all the associated Hamiltonians are decreasing in time [40,42]. For this peakon–antipeakon problem, we numerically demonstrate the total annihilation process rather than the total recovery scenario that is typical of the peakon–peakon problem.

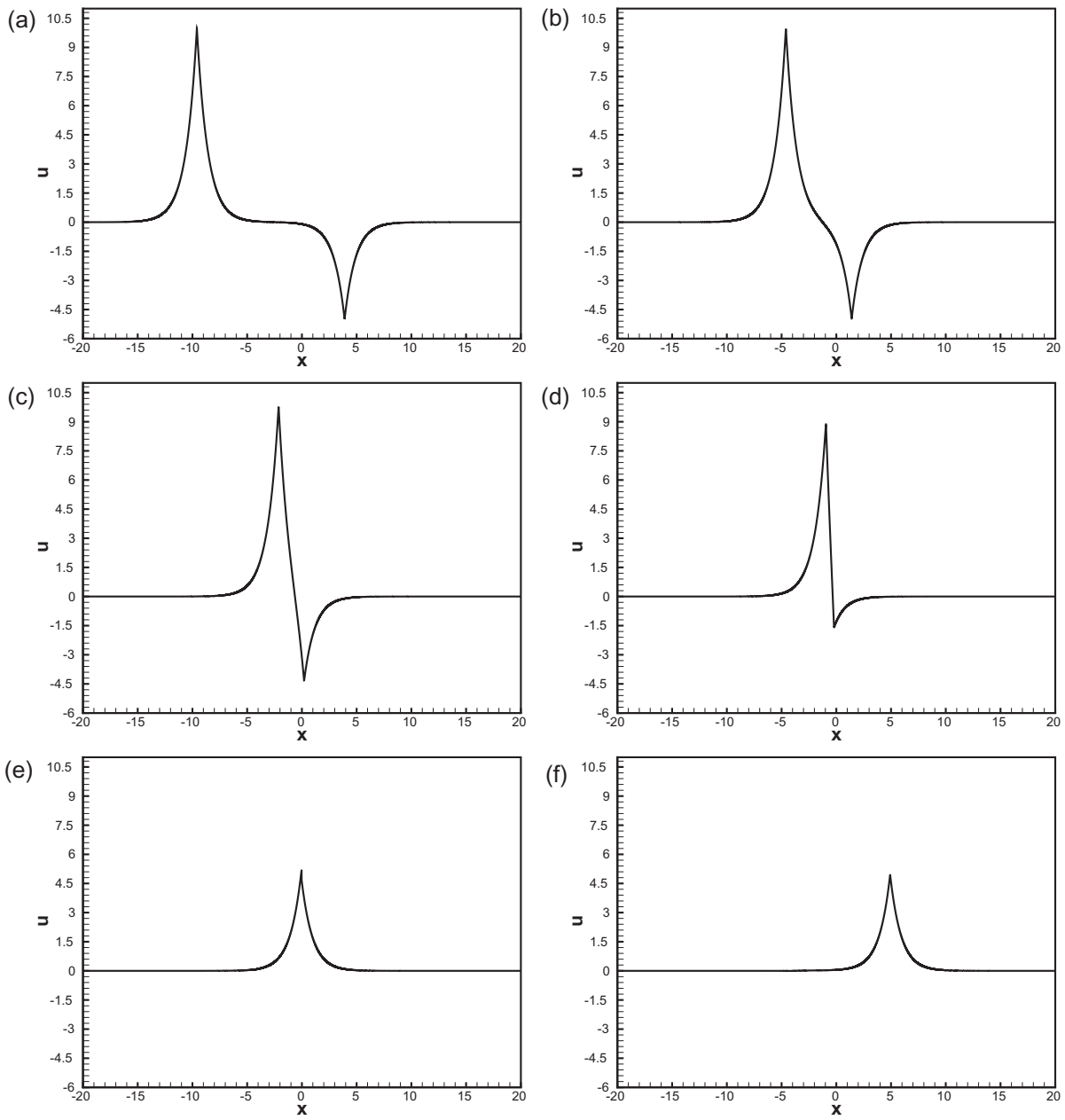


**Fig. 6.** The predicted one-peakon and one-antipeakon interaction solutions in a domain of 32,768 grids at different times. (a) $t = 0.0$; (b) $t = 0.5$; (c) $t = 0.75$; (d) $t = 0.875$; (e) $t = 1.0$; (f) $t = 2.0$.

### 7.3. Two-peakon and one-antipeakon interaction problem

We also solve the problem, that is subject to the periodic boundary condition, with the initial condition given below in a domain of $-15 \leqslant x \leqslant 45$

$$u(x, t = 0) = 5\exp(-|x|) + \exp(-|x - 20|) - 2\exp(-|x - 35|) \tag{49}$$

This problem can be considered as the combination of the peakon–peakon and peakon–antipeakon two problems. Based on the solutions plotted in Fig. 10 in the domain of 16,384 nodal points, we can get the value of $H_1$, plotted in Fig. 11, that decreases in time. This exhibits thus also the globally dissipative solution behavior after the collision of the peakons and antipeakon. Also, the Hamiltonian $H_2$ is seen to decrease its magnitude at about the same time when $H_1$ decreases sharply. Mass is still conserved quite well all the time.

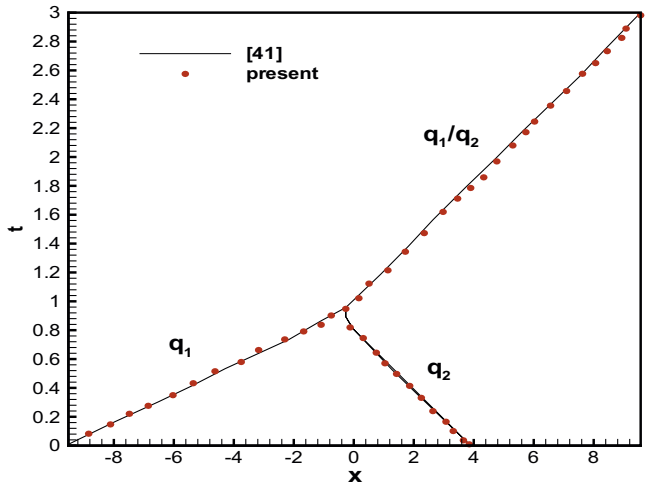


**Fig. 7.** Comparison of the predicted positions of the peaks. $q_1/q_2$ means the peak position for the wave after the collision of peakon ($q_1$) and antipeakon ($q_2$).

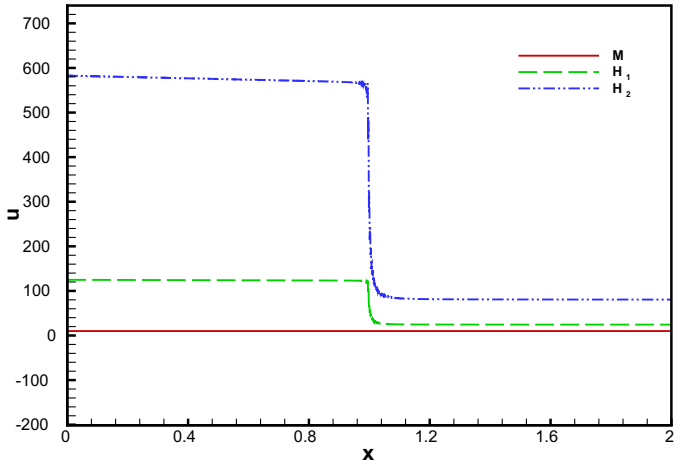


**Fig. 8.** The values of $M = \int_{-\infty}^{+\infty} u\,dx$, $H_1 = \frac{1}{2}\int_{-\infty}^{+\infty}(u^2 + u_x^2)dx$ and $H_2 = \frac{1}{2}\int_{-\infty}^{+\infty}(u^3 + uu_x^2 + 2\kappa u^2)dx$ are plotted against time for the investigated peakon–antipeakon problem.

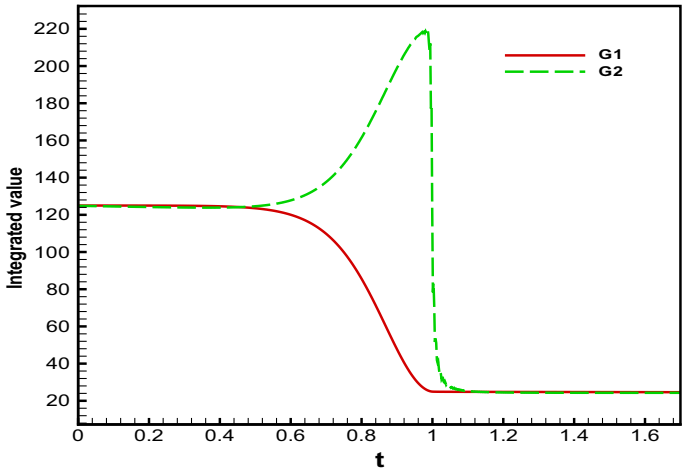


**Fig. 9.** The computed results of $G_1 (= \int_{-\infty}^{+\infty} u^2\,dx)$ and $G_2 (= \int_{-\infty}^{+\infty} u_x^2\,dx)$ are plotted against time.

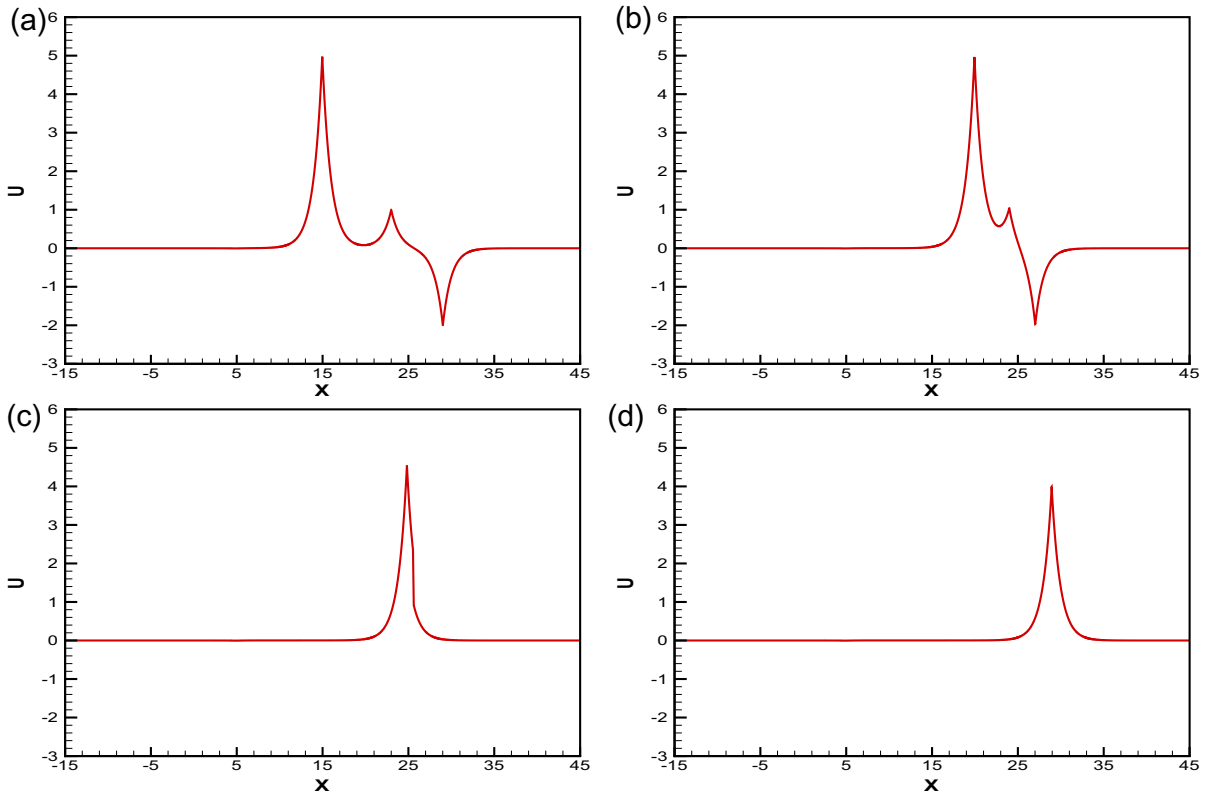


**Fig. 10.** The predicted solutions for the problem, subject to the initial condition Eq. (49), in the domain of 16,384 grids at different times. (a) $t = 3.0$; (b) $t = 4.0$; (c) $t = 5.0$; (d) $t = 6.0$.

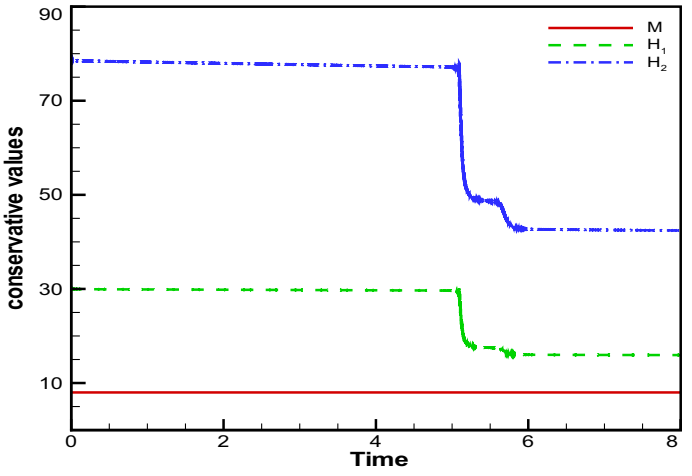


**Fig. 11.** The predicted values of $M = \int_{-\infty}^{+\infty} u\,dx$, $H_1 = \frac{1}{2}\int_{-\infty}^{+\infty}(u^2 + u_x^2)dx$ and $H_2 = \frac{1}{2}\int_{-\infty}^{+\infty}(u^3 + uu_x^2 + 2\kappa u^2)dx$ that are plotted against time for the problem given in Section 7.3.

### 7.4. Three-peakon and one-antipeakon interaction problem

We also consider the three-peakon and one-antipeakon case which was studied previously by Holden and Raynaud [41]. This problem, which initially involves three right-running peakons and one left-running antipeakon, will be solved in the domain $-20 \leqslant x \leqslant 20$

$$u(x, t = 0) = p_1(t)e^{-|x-q_1(t)|} + p_2(t)e^{-|x-q_2(t)|} + p_3(t)e^{-|x-q_3(t)|} + p_4(t)e^{-|x-q_4(t)|} \tag{50}$$

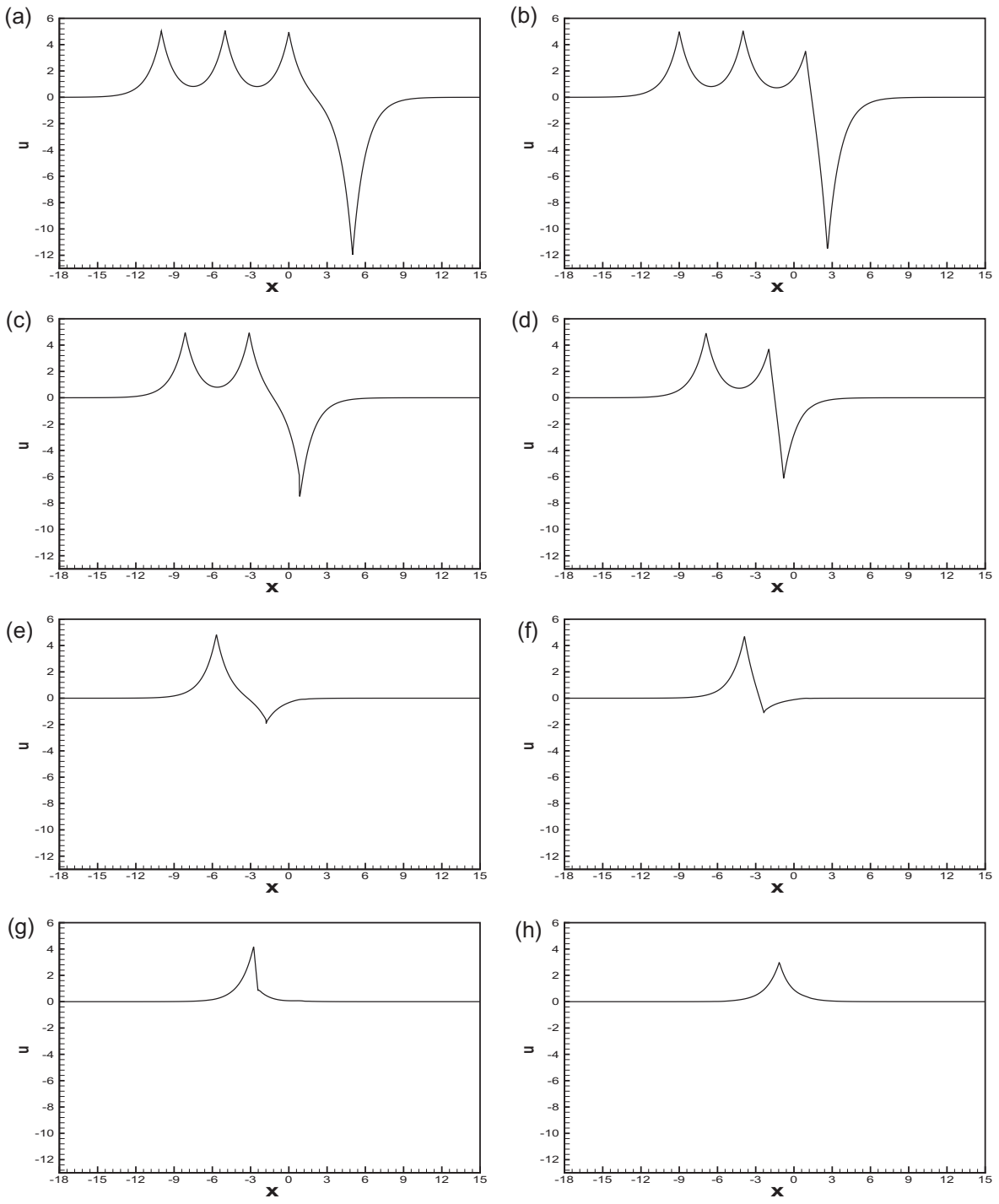


**Fig. 12.** The predicted three-peakon and one-antipeakon interaction solutions in a domain of 8192 nodal points at different times. (a) $t = 0.2$; (b) $t = 0.375$; (c) $t = 0.625$; (d) $t = 0.875$; (e) $t = 1.0$; (f) $t = 1.125$; (g) $t = 1.5$; (h) $t = 2.0$.

In the above, $q_1$, $q_2$, $q_3$ and $q_4$ are chosen to be $(q_1, q_2, q_3, q_4) = (-10, -5, 0, 5)$. Subject to the periodic boundary condition, CH equation will be solved at $p_1 = 5$, $p_2 = 5$, $p_3 = 5$ and $p_4 = -12$ [41]. The predicted solutions in the domain of 8192 nodal points plotted in Fig. 12 compare well with the results given in [41]. In Fig. 13 one can see that our predicted locations of the peakons and antipeakon agree also quite well with those given in [41]. We, as before, plot the values of $M_1$, $H_1$ and $H_2$ against time in Fig. 14 to exhibit the globally dissipative multipeakon–antipeakon solution.

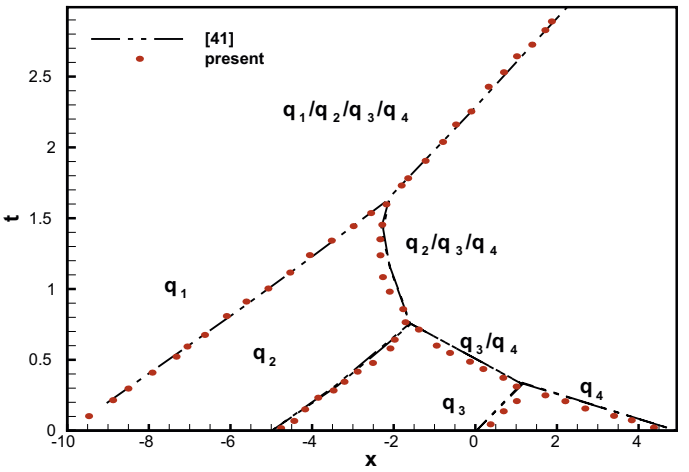


**Fig. 13.** Comparison of the predicted positions of the peaks.

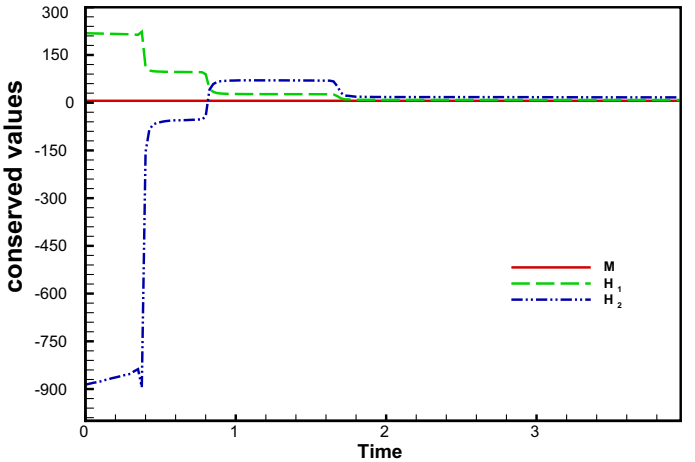


**Fig. 14.** The computed values of $M = \int_{-\infty}^{+\infty} u\,dx$, $H_1 = \frac{1}{2}\int_{-\infty}^{+\infty}(u^2 + u_x^2)dx$ and $H_2 = \frac{1}{2}\int_{-\infty}^{+\infty}(u^3 + uu_x^2 + 2\kappa u^2)dx$ against time for the investigated three-peakon and one-antipeakon interaction problem.

## 8. Concluding remarks

To reduce the differential order, in this study the Camassa–Holm equation is recast to its equivalent $u - m$ and $u - P$ formulations. Moreover, the space–time mixed derivative term in the Camassa–Holm equation is eliminated to simplify the computational study. In both formulations, we approximate the time derivative term by the sixth-order accurate implicit symplectic Runge–Kutta scheme to preserve the conserved quantities in the Camassa–Holm equation. As for the first-order spatial derivative terms shown in both formulations, the dispersion error predicted from the proposed fifth-order accurate combined compact scheme is minimized. We validate both formulations and assess their computational performances in terms of the numerical accuracy. It can be found through the analytic test problem that the $u - P$ formulation outperforms the $u - m$ formulation. For the single peakon problem, both mass and Hamiltonians can be perfectly conserved all the time. For the peakon–peakon interaction problem, the simulation results clearly exhibit mass exchange between the two peakons that propagate along the same direction without exhibiting wave breaking. While mass exchange between the individual peakons of different heights is found, the total mass and Hamiltonians remain almost unchanged with time when the higher peakon, which moves faster than the lower one, overtakes the slower-moving peakon. As a result, we numerically confirm the switching scenario in the Camassa–Holm equation. For the peakon–antipeakon problem, after the collision time the Hamiltonians $H_1$ and $H_2$ decrease sharply. The Camassa–Holm equation, which permits a globally dissipative solution, is therefore numerically demonstrated. Mass remains, however, unchanged before as well as after the collision of the peakons and antipeakon.

## Acknowledgements

This research is supported by National Science Council through the Grants NSC 98-2628-M-002-006 and 98-2811-E-002-006. The first author would like to express thanks to Prof. Long Lee (Department of Mathematics, University of Wyoming, Laramie, USA) for his fruitful discussion in the course of conducting this study.

## References

[1] R. Camassa, D. Holm, An integrable shallow water equation with peaked solitons, Phys. Rev. Lett. 71 (1993) 1661–1664.
[2] H.H. Dai, Exact travelling-wave solutions of an integrable equation arising in hyperelastic rods, Wave Motion 28 (4) (1998) 367–381.
[3] D.D. Holm, M.F. Staley, Wave structure and nonlinear balances in a family of evolutionary PDEs, SIAM J. Appl. Dyn. Syst. 2 (2003) 323–380.
[4] A. Degasperis, M. Procesi, in: A. Degasperis, G. Gaeta (Eds.), Asymptotic Integrability, Symmetry and Perturbation Theory, World Scientific Publishing, 1999, pp. 23–27.
[5] A. Constantin, J. Escher, Wave breaking for nonlinear shallow water equations, Acta Math. 181 (1998) 229–243.
[6] Y. Xu, C.W. Shu, A local discontinuous Galerkin method for the Camassa–Holm equation, SIAM J. Numer. Anal. 46 (4) (2008) 1998–2021.
[7] T.J. Bridges, S. Reich, Multi-symplectic integrators: numerical schemes for Hamiltonian PDE that conserve symplecticity, Phys. Lett. A 284 (4–5) (2001) 184–193.
[8] D. Cohen, B. Owren, X. Raynaud, Multi-symplectic integration of the Camassa–Holm equation, J. Comput. Phys. 227 (2008) 5492–5512.
[9] M. Stanislavova, A. Stefanov, On global finite energy solutions of the Camassa–Holm equation, J. Fourier Anal. Appl. 11 (5) (2005) 511–531.
[10] G.M. Coclite, K.H. Karlsen, N.H. Risebro, A convergent finite difference scheme for the Camassa–Holm equation with general $H^1$ initial data, SIAM J. Numer. Anal. 46 (3) (2008) 1554–1579.
[11] A. Bressan, A. Constantin, Global conservative solutions of the Camassa–Holm equation, Arch. Ration. Mech. Anal. 183 (2) (2007) 215–239.
[12] S. Hakkaev, Stability of peakons for an integrable shallow water equation, Phys. Lett. A 354 (1–2) (2006) 137–144.
[13] J. Lenells, Stability of periodic peakons, Int. Math. Res. Notices 10 (2004) 485–499.
[14] J. Lenells, Conservation laws of the Camassa–Holm equation, J. Phys. A 38 (2005) 869–880.
[15] A. Constantin, Existence of permanent and breaking waves for a shallow water wave equation: a geometric approach, Ann. Inst. Fourier (Grenoble) 50 (2000) 321–362.
[16] H. Holden, X. Raynaud, Global conservative solutions of the Camassa–Holm equation – a Lagrangian point of view, Commun. Partial Diff. Equat. 32 (10–12) (2007) 1511–1549.
[17] A.S. Fokas, B. Fuchssteiner, On the structure of symplectic operators and hereditary symmetries, Lett. Nuovo Cimento 28 (1980) 299–303.
[18] B. Fuchssteiner, A.S. Fokas, Symplectic structures, their Bäcklund transformations and hereditary symmetries, Physica D 4 (1) (1981) 47–66.
[19] K. El Dika, Asymptotic stability of solitary waves for the Benjamin–Bona–Mahony equation, Discrete Contin. Dyn. Syst. 3 (3) (2005) 583–662.
[20] R. Camassa, L. Lee, A complete integral particle method for a nonlinear shallow-water wave equation in periodic domains, DCDIS, Series A 14 (S2) (2007) 1–5.
[21] R. Camassa, Characteristics and initial value problem of a completely integrable shallow water equation, DCDs-B 3 (2003) 115–139.
[22] R. Camassa, J. Huang, L. Lee, On a completely integral numerical solution for a nonlinear shallow-water wave equation, J. Nonlinear Math. Phys. 12 (2005) 146–162.
[23] R. Camassa, J. Huang, L. Lee, Integral and integrable algorithm for a nonlinear shallow-water wave equation, J. Comput. Phys 216 (2006) 547–572.
[24] H. Holden, X. Raynaud, A convergent numerical scheme for the Camassa–Holm equation based on multipeakons, Discrete Contin. Dyn. Syst. 14 (2006) 503–523.
[25] H. Holden, X. Raynaud, Convergence of a finite difference scheme for the Camassa–Holm equation, SIAM J. Numer. Anal. 44 (2006) 1655–1680.
[26] H. Kalisch, J. Lenells, Numerical study of traveling-wave solutions for the Camassa–Holm equation, Chaos Solitons Fract. 25 (2005) 287–298.
[27] H. Kalisch, X. Raynaud, Convergence of a spectral projection of the Camassa–Holm equation, Numer. Methods Partial Diff. Equat. 22 (2006) 1197–1215.
[28] R. Artebrant, H.J. Schroll, Numerical simulation of Camassa–Holm peakons by adaptive upwinding, Appl. Numer. Math. 56 (2006) 695–711.
[29] T. Matsuo, H. Yamaguchi, An energy-conserving Galerkin scheme for a class of nonlinear dispersive equations, J. Comput. Phys. 228 (2009) 4346–4358.
[30] B.-F. Feng, K. Maruno, Y. Ohta, A self-adaptive mesh method for the Camassa–Holm equation, J. Comput. Appl. Math. 235 (1) (2010) 229–243.
[31] P.H. Chiu, L. Lee, T.W.H. Sheu, A dispersion–relation-preserving algorithm for a nonlinear shallow-water wave equation, J. Comput. Phys. 228 (2009) 8034–8052.
[32] Y. Ohta, K-I. Maruno, B.-F. Feng, An integrable semi-discretization of the Camassa–Holm equation and its determinant solution, J. Phys. A: Math. Theor. 41 (2008) 355205.
[33] P.H. Chiu, L. Lee, T.W.H. Sheu, A sixth-order dual preserving algorithm for the Camassa–Holm equation, J. Comput. Appl. Math. 233 (2010) 2267–2278.
[34] W. Oevel, W. Sofroniou, Symplectic Runge–Kutta schemes II: classification of symplectic methods, Univ. of Paderborn, Germany, Preprint, 1997.
[35] P.C. Chu, C. Fan, A three-point combined compact difference scheme, J. Comput. Phys. 140 (1998) 370–399.
[36] C.K.W. Tam, J.C. Webb, Dispersion–relation-preserving finite difference schemes for computational acoustics, J. Comput. Phys. 107 (1993) 262–281.
[37] A. Parker, Y. Matsuno, The peakon limits of soliton solutions of the Camassa–Holm equation, J. Phys. Soc. Jpn. 75 (12) (2006) 124001.
[38] J. Lenells, Traveling wave solutions of the Camassa–Holm equation, J. Diff. Equat. 217 (2005) 393–430.
[39] A. Chen, J. Li, Single peak solitary wave solutions for the osmosis $\kappa(2,2)$ equation under inhomogeneous boundary condition, J. Math. Anal. Appl. 369 (2010) 758–766.
[40] A. Bressan, A. Constantin, Global dissipative solutions of the Camassa–Holm equation, Anal. Appl. 5 (1) (2007) 1–27.
[41] H. Holden, X. Raynaud, Global dissipative multipeakon solutions of the Camassa–Holm equation, Commun. Partial Diff. Equat. 33 (11) (2008) 2040–2063.
[42] H. Holden, X. Raynaud, Dissipative solutions for the Camassa–Holm equation, Discrete Contin. Dyn. Syst. 24 (4) (2009) 1047–1112.